



1 **Impact of aerosol hygroscopic growth on retrieving aerosol extinction coefficient
2 profiles from elastic-backscatter lidar signals**

3 Gang Zhao¹, Chunsheng Zhao¹, Ye Kuang¹, Jiangchuan Tao¹, Wangshu Tan¹, Yuxuan Bian², Jing Li¹,
4 Chengcai Li¹

5 1 Department of Atmospheric and Oceanic Sciences, School of Physics, Peking University, Beijing,
6 China

7 2 State Key Laboratory of Severe Weather, Chinese Academy of Meteorological Sciences, Beijing,
8 100081, China

9 *Correspondence to: Chunsheng Zhao (zcs@pku.edu.cn)*

10 **Abstract**

11 Light detection and ranging (lidar) measurements have been widely used to profile ambient
12 aerosol extinction coefficient (σ_{ext}). Particle extinction-to-backscatter ratio (lidar ratio, LR), which
13 highly depends on aerosol dry particle number size distribution (PNSD) and aerosol hygroscopicity, is
14 introduced to retrieve the σ_{ext} profile from elastic-backscatter lidar signals. Conventionally, a constant
15 column integrated LR that is estimated from aerosol optical depth is used by the retrieving algorithms.
16 In this paper, the influences of aerosol PNSD, aerosol hygroscopic growth and relative humidity (RH)
17 profiles on the variation of LR are investigated based on the datasets from field measurements in the
18 North China Plain (NCP). Results show that LR has an enhancement factor of 2.2 when RH reaches
19 92%. Simulation results indicate that both the magnitude and vertical structures of the σ_{ext} profiles by
20 using column-related LR method are significantly biased from the original σ_{ext} profile. The relative
21 bias, which is mainly influenced by RH and PNSD, can reach up to 40% when RH at the top of the
22 mixed layer is above 90%. A new algorithm for retrieving σ_{ext} profiles and a new scheme of LR
23 enhancement factor by RH in the NCP are proposed in this study. The relative bias between the σ_{ext}
24 profile retrieved with this new algorithm and the ideal true value is reduced to below 13%.

25 **1. Introduction**

26 Atmospheric aerosols can directly scatter and absorb solar radiation, thus exerting significant
27 impacts on the atmospheric environment and climate change. Vertical distributions of aerosol particles
28 are crucial for studying the roles of atmospheric aerosols in the radiation balance of the
29 Earth-Atmosphere system (Kuang et al., 2016), air pollution transportation (Gasteiger et al., 2017) and



30 boundary layer process. However, there remain many problems while determining the spatial and
31 temporal distributions of aerosols because of their highly variable properties (Anderson and Anderson,
32 2003; Andreae and Crutzen, 1997) and complex sources. As a result, our knowledge about the vertical
33 distributions of aerosols is still very limited.

34 Light detection and ranging (lidar) instruments are useful remote sensing tools to monitor profiles
35 of aerosol optical properties. This kind of instrument involves a pulsed laser beam, which can be used
36 to detect the back-scatter signals from aerosols and air molecules in the atmosphere (Klett, 1981).
37 Elastic-backscatter lidar is one of the most frequently used instruments (He et al., 2006; Pietruczuk and
38 Podgórski, 2009). However, there are some limitations when deriving aerosol extinction coefficient
39 (σ_{ext}) and aerosol back scattering coefficient (β_{sca}) from elastic-backscatter lidar signals. Many efforts
40 have been carried out to retrieve the σ_{ext} profiles from lidar signals (Klett, 1981, 1985). Particle
41 extinction-to-backscatter ratio, which is usually termed as the lidar ratio (LR), is required when
42 retrieving σ_{ext} profiles (Fernald, 1984; Fernald et al., 1972). LR can be derived directly using Raman
43 lidar (Pappalardo et al., 2004b) and high spectral resolution lidar (She et al., 1992; Shipley et al., 1983;
44 Sroga et al., 1983) measurements. Raman lidar has low signal to noise ratios (SNR) during the day,
45 which may lead to significant bias and uncertainties in retrieving lidar signals. High spectral resolution
46 lidar have high technique requirement and expensive first cost. (Ansmann et al., 2002) demonstrated
47 that the profile of LR could be retrieved from Raman lidar and this LR profile can be used to retrieve
48 σ_{ext} profiles from high SNR elastic-backscattering lidar data. However, there exist many cases when
49 elastic-backscatter lidar is used without concurrently measured LR profile.

50 Sun-photometer, radiometer and elastic-backscatter lidar data are usually used simultaneously to
51 retrieve σ_{ext} profiles (Chaikovsky et al., 2016; He et al., 2006). In these studies, σ_{ext} profiles could be
52 retrieved from elastic-backscatter lidar signals by using a constant column-related LR, which is
53 constrained by measurements of aerosol optical depth (AOD) from sun-photometer. However, many
54 factors such as aerosol particle number size distribution (PNSD), aerosol refractive index, aerosol
55 hygroscopicity and ambient relative humidity (RH), have large influences on LR. It is found that the
56 ratio of σ_{ext} and β_{sca} grows linearly but slowly as RH increases when RH is lower than 80% (Salemink
57 et al., 1984). Different types of aerosols may correspond to different behaviors of LR under different
58 conditions (Ackermann, 1998). Further research found that LR is likely to change significantly due to
59 the substantial variation of RH in the mixed layer (Ferrare et al., 1998). Small errors from the initial



60 conditions may lead to large bias of retrieved σ_{ext} profiles (Sušnik et al., 2014). It is likely that using a
61 constant LR profile instead of variable LR profile to retrieve elastic-backscatter lidar data may result in
62 significant bias of retrieved σ_{ext} profiles. The sounding profiles show that RH is highly variable and
63 frequently beyond 80% in the mixed layer in the NCP (Kuang et al., 2016) which is one of the most
64 polluted areas around the world (Ma et al., 2011; Xu et al., 2011). According to this, it is interesting to
65 know how much σ_{ext} profiles retrieved from elastic-backscatter lidar signals will be deviated if
66 constant column-related LR profile is used in the NCP. Few works have been done to assess the bias of
67 using a constant LR profile.

68 In this research, influences of aerosol hygroscopic growth on LR by using Mie theory (Bohren and
69 Huffman, 2007a) and κ -Köhler theory (Petters and Kreidenweis, 2007) are studied and a further
70 discussion about impacts of RH profiles on LR profiles are carried out. Several simulations are
71 performed to study how much the σ_{ext} profiles will be affected if constant column-related LR profiles
72 are used. Sensitivity tests are also carried out to investigate the variability of the bias caused by using
73 constant column-related LR profiles under different pollution levels. Based on conducted analysis, a
74 feasible method is proposed to decrease the bias of σ_{ext} profiles retrieved from the elastic-backscatter
75 lidar signals. Finally, real-time field measurements of micro-pulsed lidar (MPL) signals are used to
76 validate this method.

77 **2. Data**

78 **2.1 Datasets of aerosol properties**

79 During the first period of Haze in China (HaChi) campaign
80 (http://www.atmos-chem-phys.net/special_issue226.html), the physical and chemical properties of
81 aerosol particles were measured at the Wuqing meteorological station. Wuqing site is located between
82 two megacities (Beijing and Tianjin) of NCP, and can represent the pollution conditions of the NCP
83 (Xu et al., 2011). This study uses the measured datasets of PNSD, black carbon (BC) (Ma et al., 2012)
84 and aerosol hygroscopicity (Chen et al., 2014; Liu et al., 2014) during the field campaign. Details
85 about this field campaign and instruments used can be found in the references.

86 **2.2 RH profiles**

87 The intensive GTS1 observation (Bian et al., 2011) at the meteorological bureau of Beijing (39°48'
88 N, 116°28' E) were carried out from July to September in 2008. With a resolution of 10m in the vertical
89 direction, the radiosonde data includes profiles of temperature, pressure and RH. During the intensive



90 observation period, balloon soundings were performed four times a day.

91 Water vapor mixing ratio is almost constant in the mixed layer due to extensive turbulent mixing
92 existing and decreases rapidly above the mixed layer. RH profiles that exhibit well-mixed vertical
93 structures are picked out and studied. With this, the maximum RH in the vertical direction can be used
94 as a good representation of RH profiles. RH profiles are classified into four typical groups based on the
95 maximum RH ranges: 60%-70%, 70%-80%, 80%-90% and 90%-95% (Kuang et al., 2016). These four
96 kinds of typical well-mixed RH profiles are labeled as P60-70, P70-80, P80-90 and P90-95
97 respectively.

98 **2.3 MPL signals**

99 A single wavelength polarization diversity elastic lidar system is installed on the roof of the
100 physics building in Peking University. This instrument is a MPL manufactured by Sigma Space, using
101 a Nd: YVO4 532nm pulsed DC10H-532SS laser source, with a pulse duration of 10.3ns, energy of
102 6-8uJ and a repetition of 2500Hz. It collects elastically backscattered signals from the atmosphere by
103 separately detecting its parallel and cross polarization components with respect to the polarization of
104 laser. Concurrently measured AOD data comes from the AERONET BEIJING_PKU station, which is
105 located at the same place as the Lidar.

106 **3. Methodology**

107 **3.1 Influences of aerosol hygroscopic growth on LR**

108 In this research, the Mie model (Bohren and Huffman, 2007a) is used to study the influence of RH
109 on LR. When running the Mie model, aerosol PNSD, aerosol complex refractive index, RH, black
110 carbon mixing state and black carbon concentration are essential.

111 Mixing states of BC come from the measurement during the Hachi Campaign. In previous work,
112 BC mixing states during the Hachi campaign were presented as both core-shell mixed and externally
113 mixed (Ma et al., 2012). Ma et al. (2012) provides the ratio of BC mass concentration under externally
114 mixed state to total BC mass concentration as follows:

$$115 \quad r_{ext_BC} = \frac{M_{ext_BC}}{M_{BC}} \quad (1).$$

116 M_{ext_BC} is the mass concentration that is externally mixed and M_{BC} is the total mass concentration of
117 BC. The mean value of r_{ext_BC} is used as a representation of the mixing state in this study. The
118 size-resolved distribution of BC mass concentration is the same as that used by Ma et al (2012a).



119 As for the aerosol hygroscopicity, the size-resolved hygroscopicity parameter κ (Petters and
120 Kreidenweis, 2007) introduced in (Chen et al., 2012) is used to account for aerosol hygroscopic growth.
121 The size-resolved hygroscopicity parameter κ is derived from the aerosol hygroscopic growth factor
122 measured by High Humidity Tandem Differential Mobility Analyzer. Size-resolved κ with high time
123 resolution is derived by using the HaChi Campaign measurement data (Chen et al., 2012; Liu et al.,
124 2011). The mean value of size-resolved κ is used to account for the mean hygroscopicity of aerosols in
125 this study.

126 The refractive index (\tilde{m}) considering the water content in the particle, is derived as a volume
127 mixture between the dry aerosol and water (Wex et al., 2002):

$$128 \quad \tilde{m} = f_{V,dry} \tilde{m}_{aero,dry} + (1 - f_{V,dry}) \tilde{m}_{water} \quad (2).$$

129 $f_{V,dry}$ is the ratio of the dry aerosol volume to total aerosol volume at given RH condition; $\tilde{m}_{aero,dry}$ is
130 the refractive index of dry ambient aerosols and \tilde{m}_{water} is the refractive index of water content
131 absorbed by aerosols.

132 For each measured aerosol PNSD under dry condition, the corresponding aerosol PNSD at a given
133 RH can be calculated. Aerosol refractive index can be determined, too. With this information, LR can
134 be obtained. Different LR values under different RH conditions are available.

135 The LR enhancement factor is introduced to describe the influence of aerosol hygroscopic growth
136 on LR at different RH. It is defined as the ratio of LR at a given RH to LR at the condition of
137 RH<40%.

138 **3.2 LR profiles and σ_{ext} profiles**

139 Assumptions about aerosol properties in the vertical direction are made to calculate LR profiles
140 and σ_{ext} profiles.

141 Liu et al. (2009) studied vertical profiles of aerosol total number concentration (Na) with aircraft
142 measurements. Vertical distributions of Na are parameterized according to the vertical distribution
143 properties of Na. Results showed that Na is relatively constant in the mixed layer. A transition layer
144 where Na linearly decreases exists in the parameterized scheme. Na also exponentially decreases
145 above the transition layer. The same parameterized scheme proposed by Liu et al. (2009) is adopted by
146 this study. Both the study of Liu et al. (2009) and Ferrero et al. (2010) manifests that the dry aerosol
147 PNSD in the mixed layer varies little. The shape of dry aerosol PNSD is assumed constant along with
148 the height, which means that aerosol PNSD at different heights divided by Na give the same



149 normalized PNSD.

150 As for the BC vertical distribution, Ferrero et al. (2011) and Ran et al. (2016) demonstrate that BC
151 mass concentration in the mixed layer remains relatively constant and decreases sharply above the
152 mixed layer. According to this, parameterization scheme of BC vertical distributions is assumed the
153 same as that of the aerosol. The shape of the size-resolved BC mass concentration distribution is also
154 assumed the same as that at the surface.

155 LR profiles and σ_{ext} profiles can be calculated by Mie theory under these assumptions. Details of
156 computing σ_{ext} profiles can be found at Kuang et al. (2015).

157 **3.3 Simulated elastic-backscatter lidar signals**

158 The intensity of signals received by elastic-backscatter lidar depends on optical properties of
159 objects and the distance between scattering objects and receiving system. It can be typically described
160 by the following formula:

$$161 \quad P(R) = C \times P_0 \times \frac{\beta(R)}{R^2} \times e^{\int_0^R -2 \times \sigma(r) \times dr} \quad (3).$$

162 In equation (3), P_0 is the intensity of the laser pulse. R is the spatial distance between scattering
163 objects and the receiving system. C is a correction factor determined by the status of
164 elastic-backscatter lidar machine itself. $\beta(R)$ refers to the sum of aerosol backscattering coefficient
165 (β_{sca}) and air molecule backscattering coefficient ($\beta_{\text{sca,mole}}$) at distance R . $\sigma(R)$ denotes the sum of σ_{ext}
166 and air molecule's extinction coefficient ($\sigma_{\text{ext,mole}}$). $\beta_{\text{sca,mole}}$ and $\sigma_{\text{ext,mole}}$ can be calculated by using
167 Rayleigh scattering theory when the temperature and pressure are available.

168 In this study, we can theoretically get the intensities of elastic-backscatter lidar signals from each
169 given σ_{ext} and β_{sca} profiles with the assumption that C is equal to one. Retrieving elastic-backscatter
170 lidar signals can result in exactly the same σ_{ext} profile as the original one when the profile of LR is
171 available. However, a constant column-related LR profile is used to retrieve elastic-backscatter lidar
172 signals and the retrieved σ_{ext} profile would deviate from the given σ_{ext} profile when there is insufficient
173 information about the LR profile.

174 **3.4 Retrieving σ_{ext} profiles from elastic-backscatter lidar signals**

175 **3.4.1 Retrieving σ_{ext} profiles by using constant column-related LR profile method**

176 Additional information is needed to get the mathematical results of formula (3) because there are
177 two unknown parameters (β_{sca} and σ_{ext}). The commonly used method of solving this formula is to



178 assume a constant value of column-related LR and then the profiles of σ_{ext} and β_{ext} can be retrieved
179 (Fernald, 1984; Klett, 1985). Different values of column-related LR can lead to different σ_{ext} profiles
180 and different AOD. A constant column-related LR can be constrained if sun photometer are
181 concurrently measuring the AOD (He et al., 2006; Pietruczuk and Podgorski, 2009). Thus, σ_{ext} profile
182 can be retrieved by using the column-related constant LR profile.

183 **3.4.2 Retrieving σ_{ext} profiles accounting for aerosol hygroscopic growth**

184 A new method of retrieving σ_{ext} profiles from elastic-backscatter lidar signals is proposed, in
185 which the variation of LR with RH can be taken into consideration. A schematic diagram of this
186 method is shown in Fig.1. A parameterized LR profile is used to retrieve σ_{ext} profiles instead of an
187 AOD-constrained constant LR profile. Firstly, the LR enhancement factor are statistically studied and
188 parameterized under different polluted conditions. LR profile can be calculated using RH profile and
189 LR value at dry state. σ_{ext} profile can be retrieved with combination of LR profile and formula (3). Dry
190 state LR value can be constrained by comparing the integrated AOD value of retrieved σ_{ext} profile and
191 concurrently measured AOD value. LR profile is determined and σ_{ext} profile can be retrieved with the
192 constrained dry state LR.

193 **4. Results and Discussion**

194 **4.1 LR properties**

195 **4.1.1 Variation of LR with RH**

196 During the field campaign of Hachi, there were a total of 3540 different aerosol PNSDs. LR is
197 calculated by using different aerosol PNSD and RH values between 30% and 95%.

198 Relationships between dry state LR and concurrently measured σ_{ext} (sum of the aerosol scattering
199 and absorption) are shown in Fig. 2(a). It shows that LR can vary across a wide range from 30 sr to 90
200 sr, which is consistent with the literature values of continent aerosols (Ansmann et al., 2001;
201 Pappalardo et al., 2004a). This also indicates that calculating the LR by using Mie theory is feasible.
202 Fig. 2(b) gives the probability distribution function of the LR. Most of the LR lies in the range between
203 45~65 sr.

204 In order to have a better understanding of the relationship between aerosol PNSD and LR,
205 lognormal distributions of aerosol PNSD are used to fit the PNSD of aerosol particles. Firstly, the sum
206 of four different lognormal modes, which are known as Nucleation mode, Aitken mode, Accumulation
207 mode and Coarse mode, are used to fit the distribution of aerosol PNSD (Chen et al., 2012; Hussein et



208 al., 2005; Mattis et al., 2002). Details of this method can be found in Chen et al. (2012). LR values at
209 different modes are accordingly calculated by using Mie scattering theory. For each aerosol PNSD, we
210 can get one LR value by using the measured aerosol PNSD, and another four LR values by using four
211 derived lognormal mode aerosols respectively. Finally, LR based on the total PNSD is regressed on
212 derived LR from the four lognormal modes.

213 Table 1 gives the statistical results of the LR range and the correlation coefficients. Results show
214 that Accumulation mode aerosol contributes the most to the LR at 61% with a mean value of 56.04 sr.
215 The LR from Aitken mode comes second, with a contribution of 19% and a mean value of 42.15 sr.
216 The Nucleation mode aerosol gives a mean LR value of 9.72 sr, which is almost the same as the LR of
217 air molecules ($\frac{8\pi}{3}$ sr) and contributes only 3% to the total LR. The Coarse mode gets 5% partition of
218 total LR with mean value of 97 sr. It can be concluded that the Accumulation mode of the aerosols
219 should be taken into account first when deriving PNSD information from the LR signals.

220 Relationships between the LR enhancement factor and RH are given in Fig. 2(c). The LR
221 enhancement factor has a mean value lower than 1.2 when the RH is lower than 70%. LR increases
222 linearly with RH when RH is lower than 80%, which is consistent with the literature (Salemink et al.,
223 1984). However, LR can be enhanced by a factor of 2.2 when the RH reaches 92% with mean
224 hygroscopicity of aerosol. There tends to be more forward scattering and less backscattering at 180°
225 when aerosol particles grow bigger according to Mie theory (Bohren and Huffman, 2007b). With this,
226 LR value is larger when the particles grow larger.

227 Mean values of LR enhancement factor are parameterized as below:

$$228 \quad RH_0 = RH - 40 \quad (4)$$

$$229 \quad LR = LR_{dry} \times (0.92 + 2.5 \times 10^{-2}RH_0 - 1.3 \times 10^{-4}RH_0^2 + 2.2 \times 10^{-5}RH_0^3) \quad (5).$$

230 This parameterization equation can be used as a representation of the mean effect of continental
231 aerosol hygroscopicity on LR.

232 **4.1.2 LR ratio profiles**

233 Fig.3 shows four different types of RH profiles and LR profiles. Fig. 3(a) shows RH profiles of
234 P60-70, P70-80, P80-90 and P90-95 respectively. In Fig. 3(a), RH values increase with height in the
235 mixed layer and decrease with height above the mixed layer. This is a result of temperature and water
236 content distributions in the vertical direction. In the mixed layer, water vapor is well mixed within the



237 mixed layer and decreases sharply above the mixed layer. P60-70 can represent the relatively dry
238 conditions on a summer afternoon. Statistical results show that P80-90 is most likely to be observed in
239 the environment. P90-95 is a very moist environment condition and its frequency of being observed is
240 second to that of the P80-90 type.

241 Profiles of LR corresponding to RH profiles of the left column are shown in Fig. 3(b). For each
242 type of LR profile, LR increases with height in the mixed layer due to the increase of RH. At the
243 ground, the mean values of LR for each RH profiles are 38.19, 38.28, 39.53 and 40.33 sr, with a
244 standard deviation of 6.20, 6.22, 6.42 and 6.45 respectively. LR changes little from 38 sr at the ground
245 to 42 sr at the top of the mixed layer when the ambient RH is low for the RH profile of P60-70.
246 However, LR grows with a mean value from 40 sr to 60 sr with a relative difference of 50% when the
247 RH is high for the RH profile of P90-95. With such high variation of LR with RH, the retrieved σ_{ext}
248 profiles might be greatly deviated when using a constant LR profile instead of a variable one.

249 The black dotted line in Fig. 3(b) is one of the constant column-related LR profiles that are used as
250 an input of retrieving σ_{ext} profiles related to the RH profile P70-80. The constant LR has a higher value
251 at the ground and a lower value at the top of the mixed layer when compared with the calculated
252 variable LR profiles.

253 During the Hachi Campaign, LR values that are calculated by using Mie theory can change from
254 30 to 55 sr within 12 hours at the ground (about 87% of initial value). With high variation of LR over
255 time, the LR profile should be updated in time to get an accurately retrieved σ_{ext} profile. Using only
256 one measurement of LR profile to retrieve the σ_{ext} profiles may lead to great bias of retrieved results
257 (Rosati et al., 2016).

258 **4.2 Bias of retrieved σ_{ext} profiles**

259 **4.2.1 Retrieved σ_{ext} profiles vs. original σ_{ext} profiles**

260 Fig. 4 provides an example of the retrieved σ_{ext} profile by using the variable LR profile method
261 and that by using the constant LR profile method. These two kinds of profiles can also be described as
262 a given parameterized σ_{ext} profile and a retrieved σ_{ext} profile from constant LR profile. In Fig. 4(a), the
263 retrieved σ_{ext} profile by using a variable LR profile method is demonstrated by solid line. Dotted line
264 shows the retrieved σ_{ext} profile by using a constant column related LR method. Fig. 4(b) shows the
265 relative bias of the two retrieved σ_{ext} profiles at each height. Fig. 4(c) and (d) are almost the same as
266 Fig. 4(a) and (b) respectively, except that the results of Fig. 4(a) and (b) come from the RH profile of



267 P70-80 while those of Fig. 4(c) and (d) come from the RH profile of P90-95.

268 It is shown in Fig. 4(a) that the retrieved σ_{ext} by using a variable LR profile method increases with
269 height at a rate of $92.25 \text{ (Mm}^{-1}\text{km}^{-1}\text{)}$ in the mixed layer, which is consistent with the aerosol loading
270 and RH distribution. However, the retrieved σ_{ext} profile by using a constant LR profile method behaves
271 differently and decreases at a rate of $-152.87 \text{ (Mm}^{-1}\text{km}^{-1}\text{)}$. The structure of σ_{ext} profiles is different by
272 using two different methods. Moreover, the retrieved σ_{ext} from RH profile of P90-95 at the top of the
273 mixed layer is significantly deviated with a relative bias of 40%.

274 Both Fig. 4(a) and (c) show that the retrieved σ_{ext} is overestimated at ground and underestimated at
275 the top of the mixed layer. From Fig 3(b), it can be concluded that the AOD-constrained constant LR is
276 larger than the calculated true LR at the ground and smaller at the top of the mixed layer. According to
277 formula (3), signals of the elastic-backscatter lidar received at any height are proportional to the
278 backscattering capability of the aerosols. When LR is larger, a larger fraction of the signals transfer
279 forward and less is scattered back. In order to receive the same amount of signal, the backscattering
280 coefficient should be larger and this can lead to the result of a larger σ_{ext} at that layer. Thus, the σ_{ext}
281 tends to be biased higher than the given parameterized σ_{ext} when the LR is larger, and vice versa.
282 Overall, the profiles retrieved by using an AOD-constrained LR can lead to a positive bias at the
283 ground and a negative bias at the top of mixed layer.

284 **4.2.2 Sensitivity Study**

285 Simulations are conducted to study the characteristics of the retrieved σ_{ext} profile bias between
286 using the constant column-related LR profile and variable LR profile. Different kinds of aerosol PNSD,
287 AOD, aerosol hygroscopicity and RH profiles are used. Aerosol PNSD data comes from the Hachi
288 Campaign field measurement. The sensitivity of the bias in aerosol hygroscopicity is evaluated by
289 changing the size-resolved κ value. Aerosols are defined to have high hygroscopicity when the aerosol
290 size-resolved κ value is one standard deviation above the mean of the size-resolved κ value. They are
291 defined as low hygroscopicity if the size-resolved κ value is one standard deviation below mean of the
292 size-resolved κ value. Four different kinds of RH profiles are also used in this sensitivity study. As
293 discussed in section 3.2.1, a negative bias at the top of the mixed layer is accompanied by a positive
294 bias at the ground and the largest bias happens at the top of the mixed layer. It is sufficient to focus on
295 the relative bias at the top of the mixed layer.

296 Statistical characteristics of the relative bias at the top of the mixed layer are shown in Fig. 5.



297 Different panels represent the results of different aerosol hygroscopicity. The left column shows the
298 results of low aerosol hygroscopicity. Middle panel shows results from mean aerosol hygroscopicity.
299 High aerosol hygroscopicity of particles results in the properties shown in the right panel. For each
300 panel, relationships between relative bias and AOD are shown. Different colors in each panel show the
301 results of different RH profiles. Filled colors represent the ranges of the relative bias at one standard
302 deviation of using different PNSD.

303 Every panel show that relative bias clearly increases with the enhancement of RH in the
304 surroundings. The relative bias has a mean value of less than 10% for RH profile of P60-70. LR has
305 little variation when the surrounding RH is low and the bias has a low value. For RH profiles of
306 P70-80 and P80-90, the relative bias increases with RH and increases strongly up to 25% when the
307 surrounding relative humidity is high. These behaviors of relative difference under difference RH
308 conditions are consistent with the change of LR with RH.

309 Filled color ranges of relative bias at given AOD and RH profile result from the variation of
310 aerosol PNSD. The LR enhancement factor can have different behavior with different aerosol PNSD
311 according to Mie scattering theory. Changing the aerosol PNSD leads to a wider range of bias when
312 the RH is higher. Fig. 5 also shows that different PNSD can change the relative bias by a mean value
313 of 10% for different polluted conditions.

314 Relative bias increases with AOD value when the AOD is low, while it remains constant when the
315 AOD is high. When AOD is low, the amount of scattered light by air molecules occupies a large
316 fraction. Air molecules have a constant LR of $\frac{8}{3}\pi$ sr according the Rayleigh scattering theory. The
317 relative bias of retrieved σ_{ext} profile is relatively small when the AOD is low. When the AOD has a
318 larger value, backscattered signals mainly depend on aerosol backscattering and the signals
319 backscattered by air molecules are negligible. Relative bias mainly reflects the impacts of aerosol
320 hygroscopicity. The mean relative bias increases from 26% to 32% at high RH conditions with the
321 increase of aerosol hygroscopicity. Aerosol hygroscopicity should be taken into account under high
322 RH conditions.

323 To sum up, RH is one of the most important factors that influence the accuracy of retrieving the
324 elastic-backscatter lidar data. Different PNSD can also lead to a large variation of relative difference.
325 The relative difference increases with the AOD when the AOD is low, but increases little when the



326 AOD is high. Under the conditions of both high values of RH and AOD, the relative bias of retrieved
327 data reaches a maximum due to the influence of aerosol hygroscopic growth.

328 **4.3 Evaluation of LR enhancement factor parameterization**

329 Simulations were carried out to test the efficiency of LR the enhancement factor parameterization
330 scheme. All of the simulations in section 4.2 were conducted again by using the method of 3.4.2. The
331 relative bias between the parameterized σ_{ext} profile and the retrieved σ_{ext} profile by using the
332 parameterized LR enhancement factor scheme are studied and summarized in Table 2. The values
333 listed in Table 2 are the mean results under different PNSD conditions. From Table 2, we can see that
334 all of the relative bias is within the range of 13%. This indicates that the new algorithm using the mean
335 LR enhancement factor parameterization scheme is robust and can decrease the bias of the retrieved
336 elastic-backscatter lidar data significantly.

337 **4.4 Retrieving the real-time measurement elastic-backscatter lidar signals**

338 MPL data and AERONET data are employed to validate the algorithm of retrieving the
339 elastic-backscatter lidar data on the day of 5 July 2016. After quality control of data processing,
340 elastic-backscatter lidar data is retrieved by using both a constant LR profile method and a
341 parameterized variable LR profile method. Fig. 6 shows the retrieved σ_{ext} profiles using two methods
342 of local time 13:00 (a) and 14:30 (b).

343 Fig. 6(a) is a typical case of the retrieved σ_{ext} profiles under high values of both RH and AOD
344 conditions. The retrieved σ_{ext} profiles by using the constant LR profile method and variable LR profile
345 method show almost the same properties as the simulations. The relative bias reaches a value of 39.3%
346 at an altitude of 1.57 km. These differences of retrieved σ_{ext} profiles may lead to a significant bias of
347 estimating the mixed layer height and have significant impact on radiative energy distribution in the
348 vertical direction. Fig. 6(b) shows the retrieved σ_{ext} profiles of different structures from the same
349 elastic-backscatter lidar data. The retrieved σ_{ext} by using variable LR profile method increases with
350 height within the mixed layer. However, the retrieved σ_{ext} by using constant LR profile decreases
351 slightly with height within the mixed layer.

352 **5 Conclusions**

353 The influence of aerosol hygroscopic growth on LR is evaluated by using Mie scattering theory.
354 Datasets used as input to Mie theory model come from the Hachi Campaign field measurements.
355 Results show that LR in the NCP mainly ranges from 30 to 90 sr, which is consistent with literature



356 values of continental aerosols. LR could be enhanced significantly under high RH conditions, with a
357 mean factor of 2.2 at 92% RH.

358 RH in the mixed layer in the NCP is frequently observed to be higher than 90%. Under these
359 conditions, large variation of LR in the vertical direction exists. This leads to significant bias of
360 retrieved σ_{ext} profile due to a constant LR profile currently used to retrieve the elastic-backscatter lidar
361 signals. The relative bias of the retrieved σ_{ext} profiles between the constant LR profile method and the
362 variable LR profile method can reach up to 40% under high RH conditions and the retrieved σ_{ext}
363 profile structure can be different under low RH conditions.

364 Sensitivity studies are carried out to test the bias of retrieved σ_{ext} profiles. The bias increases
365 linearly with RH at low RH but increases strongly at high RH. PNSD can lead to 10% standard
366 deviation of the bias. Maximum bias happens under the conditions of both high AOD and RH that
367 frequently happen in the NCP. The influence of aerosol hygroscopic growth on LR should be taken
368 into consideration when retrieving the elastic-backscatter lidar data in the NCP.

369 A new algorithm accounting for the aerosol hygroscopic growth is proposed to retrieve the
370 elastic-backscatter lidar data. A scheme of LR enhancement factor parameterization is introduced in
371 this algorithm. The bias of retrieved σ_{ext} profiles by using this algorithm can be constrained within
372 13%. Real-time measurement of MPL data is employed to validate the algorithm and the results show
373 good consistency with the simulations.

374 This research will advance our understanding of the influence of aerosol hygroscopic growth on
375 LR and help to improve the retrieval of σ_{ext} profile from elastic-backscatter lidar signals.

376

377 **Acknowledgments**

378 This work is supported by the National Natural Science Foundation of China (41590872,
379 41375134).

380

381

382 **References**

383 Ackermann, J. (1998) The Extinction-to-Backscatter Ratio of Tropospheric Aerosol: A Numerical Study. *Journal of*
384 *Atmospheric and Oceanic Technology* 15, 1043-1050.
385 Anderson, T.L., Anderson, T.L. (2003) Variability of aerosol optical properties derived from in situ aircraft measurements



386 during ACE-Asia. *Journal of Geophysical Research* 108, ACE-15-11-ACE 15-19.

387 Andreae, M.O., Crutzen, P.J. (1997) Atmospheric Aerosols: Biogeochemical Sources and Role in Atmospheric Chemistry.

388 *Science* 276, 1052-1058.

389 Ansmann, A., Wagner, F., Althausen, D., Müller, D., Herber, A., Wandinger, U. (2001) European pollution outbreaks during

390 ACE 2: Lofted aerosol plumes observed with Raman lidar at the Portuguese coast. *Journal of Geophysical Research*

391 *Atmospheres* 106, 20725-20733.

392 Ansmann, A., Wagner, F., Müller, D., Althausen, D., Herber, A., von Hoyningen-Huene, W., Wandinger, U. (2002) European

393 pollution outbreaks during ACE 2: Optical particle properties inferred from multiwavelength lidar and star-Sun photometry.

394 *Journal of Geophysical Research: Atmospheres* 107, AAC 8-1-AAC 8-14.

395 Bian, J., Chen, H., ouml, mel, H., Duan, Y. (2011) Intercomparison of humidity and temperature sensors: GTS1, Vaisala RS80,

396 and CFH. *Advances in atmospheric sciences* 28, 139-146.

397 Bohren, C.F., Huffman, D.R., (2007a) *Absorption and Scattering by an Arbitrary Particle, Absorption and Scattering of Light*

398 by Small Particles

399 Bohren, C.F., Huffman, D.R., (2007b) *Angular Dependence of Scattering, Absorption and Scattering of Light by Small*

400 *Particles*

401 Chaikovsky, A., Dubovik, O., Holben, B., Bril, A., Goloub, P., Tanre, D., Pappalardo, G., Wandinger, U., Chaikovskaya, L.,

402 Denisov, S., Grudo, J., Lopatin, A., Karol, Y., Lapyonok, T., Amiridis, V., Ansmann, A., Apituley, A., Allados-Arboledas, L.,

403 Binietoglou, I., Boselli, A., D'Amico, G., Freudenthaler, V., Giles, D., Jose Granados-Munoz, M., Kokkalis, P., Nicolae, D.,

404 Oshchepkov, S., Papayannis, A., Perrone, M.R., Pietruck, A., Rocadenbosch, F., Sicard, M., Slutsker, I., Talianu, C., De

405 Tomasi, F., Tsekeli, A., Wagner, J., Wang, X. (2016) Lidar-Radiometer Inversion Code (LIRIC) for the retrieval of vertical

406 aerosol properties from combined lidar/radiometer data: development and distribution in EARLINET. *Atmospheric*

407 *Measurement Techniques* 9, 1181-1205.

408 Chen, J., Zhao, C.S., Ma, N., Liu, P.F., Göbel, T., Hallbauer, E., Deng, Z.Z., Ran, L., Xu, W.Y., Liang, Z., Liu, H.J., Yan, P., Zhou,

409 X.J., Wiedensohler, A. (2012) A parameterization of low visibilities for hazy days in the North China Plain. *Atmos. Chem.*

410 *Phys.* 12, 4935-4950.

411 Chen, J., Zhao, C.S., Ma, N., Yan, P. (2014) Aerosol hygroscopicity parameter derived from the light scattering enhancement

412 factor measurements in the North China Plain. *Atmos. Chem. Phys.* 14, 8105-8118.

413 Fernald, F.G. (1984) Analysis of atmospheric lidar observations: some comments. *Applied Optics* 23, 652-653.

414 Fernald, F.G., Herman, B.M., Reagan, J.A. (1972) Determination of Aerosol Height Distributions by Lidar. *Journal of Applied*

415 *Meteorology* 11, 482-489.

416 Ferrare, R.A., Melfi, S.H., Whiteman, D.N., Evans, K.D., Poellot, M., Kaufman, Y.J. (1998) Raman lidar measurements of

417 aerosol extinction and backscattering: 2. Derivation of aerosol real refractive index, single-scattering albedo, and

418 humidification factor using Raman lidar and aircraft size distribution measurements. *Journal of Geophysical Research:*

419 *Atmospheres* 103, 19673-19689.

420 Ferrero, L., Mocnik, G., Ferrini, B.S., Perrone, M.G., Sangiorgi, G., Bolzacchini, E. (2011) Vertical profiles of aerosol

421 absorption coefficient from micro-Aethalometer data and Mie calculation over Milan. *Science of the Total Environment*

422 409, 2824-2837.

423 Ferrero, L., Perrone, M.G., Petraccone, S., Sangiorgi, G., Ferrini, B.S., Lo Porto, C., Lazzati, Z., Cocchi, D., Bruno, F., Greco, F.,

424 Riccio, A., Bolzacchini, E. (2010) Vertically-resolved particle size distribution within and above the mixing layer over the

425 Milan metropolitan area. *Atmospheric Chemistry and Physics* 10, 3915-3932.

426 Gasteiger, J., Groß, S., Sauer, D., Haarig, M., Ansmann, A., Weinzierl, B. (2017) Particle settling and vertical mixing in the

427 Saharan Air Layer as seen from an integrated model, lidar, and in situ perspective. *Atmospheric Chemistry and Physics* 17,

428 297-311.

429 He, Q.S., Li, C.C., Mao, J.T., Lau, A.K.H., Li, P.R. (2006) A study on the aerosol extinction-to-backscatter ratio with



430 combination of micro-pulse LIDAR and MODIS over Hong Kong. *Atmospheric Chemistry and Physics* 6, 3243-3256.

431 Hussein, T., Maso, M.D., Petäjä, T., Koponen, I.K., Paatero, P., Aalto, P.P., Hämeri, K., Kulmala, M. (2005) Evaluation of an
432 automatic algorithm for fitting the particle number size distributions. *Boreal Environment Research* 10, 337-355.

433 Klett, J.D. (1981) Stable analytical inversion solution for processing lidar returns. *Applied Optics* 20, 211-220.

434 Klett, J.D. (1985) Lidar inversion with variable backscatter/extinction ratios. *Applied Optics* 24, 1638-1643.

435 Kuang, Y., Zhao, C.S., Tao, J.C., Bian, Y.X., Ma, N. (2016) Impact of aerosol hygroscopic growth on the direct aerosol
436 radiative effect in summer on North China Plain. *Atmospheric Environment* 147, 224-233.

437 Kuang, Y., Zhao, C.S., Tao, J.C., Ma, N. (2015) Diurnal variations of aerosol optical properties in the North China Plain and
438 their influences on the estimates of direct aerosol radiative effect. *Atmos. Chem. Phys.* 15, 5761-5772.

439 Liu, H.J., Zhao, C.S., Nekat, B., Ma, N., Wiedensohler, A., van Pinxteren, D., Spindler, G., Müller, K., Herrmann, H. (2014)
440 Aerosol hygroscopicity derived from size-segregated chemical composition and its parameterization in the North China
441 Plain. *Atmospheric Chemistry and Physics* 14, 2525-2539.

442 Liu, P., Zhao, C., Zhang, Q., Deng, Z., Huang, M., Xincheng, M.A., Tie, X. (2009) Aircraft study of aerosol vertical
443 distributions over Beijing and their optical properties. *Tellus Series B-chemical & Physical Meteorology* 61, 756-767.

444 Liu, P.F., Zhao, C.S., Göbel, T., Hallbauer, E., Nowak, A., Ran, L., Xu, W.Y., Deng, Z.Z., Ma, N., Mildenberger, K., Henning, S.,
445 Stratmann, F., Wiedensohler, A. (2011) Hygroscopic properties of aerosol particles at high relative humidity and their
446 diurnal variations in the North China Plain. *Atmos. Chem. Phys.* 11, 3479-3494.

447 Ma, N., Zhao, C.S., Müller, T., Cheng, Y.F., Liu, P.F., Deng, Z.Z., Xu, W.Y., Ran, L., Nekat, B., van Pinxteren, D., Gnauk, T., Müller,
448 K., Herrmann, H., Yan, P., Zhou, X.J., Wiedensohler, A. (2012) A new method to determine the mixing state of light
449 absorbing carbonaceous using the measured aerosol optical properties and number size distributions. *Atmos. Chem. Phys.*
450 12, 2381-2397.

451 Ma, N., Zhao, C.S., Nowak, A., Müller, T., Pfeifer, S., Cheng, Y.F., Deng, Z.Z., Liu, P.F., Xu, W.Y., Ran, L., Yan, P., Göbel, T.,
452 Hallbauer, E., Mildenberger, K., Henning, S., Yu, J., Chen, L.L., Zhou, X.J., Stratmann, F., Wiedensohler, A. (2011) Aerosol
453 optical properties in the North China Plain during HaChi campaign: an in-situ optical closure study. *Atmos. Chem. Phys.* 11,
454 5959-5973.

455 Mattis, I., Ansmann, A., Müller, D., Wandinger, U., Althausen, D. (2002) Dual-wavelength Raman lidar observations of the
456 extinction-to-backscatter ratio of Saharan dust. *Geophysical Research Letters* 29, 20-21-20-24.

457 Pappalardo, G., Amodeo, A., Mona, L., Pandolfi, M., Pergola, N., Cuomo, V. (2004a) Raman lidar observations of aerosol
458 emitted during the 2002 Etna eruption. *Geophysical Research Letters* 31, 179-211.

459 Pappalardo, G., Amodeo, A., Pandolfi, M., Wandinger, U., Ansmann, A., Bösenberg, J., Matthias, V., Amiridis, V., De Tomasi,
460 F., Frioud, M., Iarlori, M., Komguem, L., Papayannis, A., Rocadenbosch, F., Wang, X. (2004b) Aerosol lidar intercomparison
461 in the framework of the EARLINET project. 3. Ramanlidar algorithm for aerosol extinction, backscatter, and lidar ratio.
462 *Applied Optics* 43, 5370-5385.

463 Petters, M.D., Kreidenweis, S.M. (2007) A single parameter representation of hygroscopic growth and cloud condensation
464 nucleus activity. *Atmos. Chem. Phys.* 7, 1961-1971.

465 Pietruczuk, A., Podgórski, J., (2009) The lidar ratio derived from sun-photometer measurements at Belsk Geophysical
466 Observatory, *Acta Geophysica*, p. 476.

467 Pietruczuk, A., Podgórski, J. (2009) The lidar ratio derived from sun-photometer measurements at Belsk Geophysical
468 Observatory. *Acta Geophysica* 57, 476-493.

469 Ran, L., Deng, Z., Xu, X., Yan, P., Lin, W., Wang, Y., Tian, P., Wang, P., Pan, W., Lu, D. (2016) Vertical profiles of black carbon
470 measured by a micro-aethalometer in summer in the North China Plain. *Atmospheric Chemistry and Physics* 16,
471 10441-10454.

472 Rosati, B., Herrmann, E., Bucci, S., Fierli, F., Cairo, F., Gysel, M., Tillmann, R., Größ, J., Gobbi, G.P., Di Liberto, L.,
473 Di Donfrancesco, G., Wiedensohler, A., Weingartner, E., Virtanen, A., Mentel, T.F., Baltensperger, U. (2016) Studying the



474 vertical aerosol extinction coefficient by comparing in situ airborne data and elastic backscatter lidar. Atmospheric
475 Chemistry and Physics 16, 4539-4554.

476 Salemink, H.W.M., Schotanus, P., Bergwerff, J.B. (1984) Quantitative lidar at 532 nm for vertical extinction profiles and the
477 effect of relative humidity. Applied Physics B 34, 187-189.

478 She, C.Y., Alvarez, R.J., Caldwell, L.M., Krueger, D.A. (1992) High-spectral-resolution Rayleigh-Mie lidar measurement
479 of aerosol and atmospheric profiles. Optics Letters 17, 541-543.

480 Shipley, S.T., Tracy, D.H., Eloranta, E.W., Trauger, J.T., Sroga, J.T., Roesler, F.L., Weinman, J.A. (1983) High spectral resolution
481 lidar to measure optical scattering properties of atmospheric aerosols. 1: Theory and instrumentation. Applied Optics 22,
482 3716-3724.

483 Sroga, J.T., Eloranta, E.W., Shipley, S.T., Roesler, F.L., Tryon, P.J. (1983) High spectral resolution lidar to measure optical
484 scattering properties of atmospheric aerosols. 2: Calibration and data analysis. Applied Optics 22, 3725-3732.

485 Sušnik, A., Holder, H., Eichinger, W. (2014) A Minimum Variance Method for Lidar Signal Inversion. Journal of Atmospheric
486 and Oceanic Technology 31, 468-473.

487 Xu, W.Y., Zhao, C.S., Ran, L., Deng, Z.Z., Liu, P.F., Ma, N., Lin, W.L., Xu, X.B., Yan, P., He, X., Yu, J., Liang, W.D., Chen, L.L. (2011)
488 Characteristics of pollutants and their correlation to meteorological conditions at a suburban site in the North China Plain.
489 Atmos. Chem. Phys. 11, 4353-4369.

490

491



492 **Table 1** Calculated LR of four lognormal modes PNSD. R^2 is the correlation coefficient of the LR from the lognormal mode PNSD
493 and LR from the total PNSD.

Mode	Diameter (nm)	LR(sr)	R^2
Nuclei mode	19.40	9.72	0.03
Aitken mode	70.11	42.15	0.19
Accumulation mode	239.90	56.04	0.61
Coarse mode	1451	92.93	0.05

494
495



496 **Table 2** Relative difference (%) of the extinction coefficient profiles between using the parameterized LR enhancement factor and
497 the presumed LR under different AOD and RH profile conditions

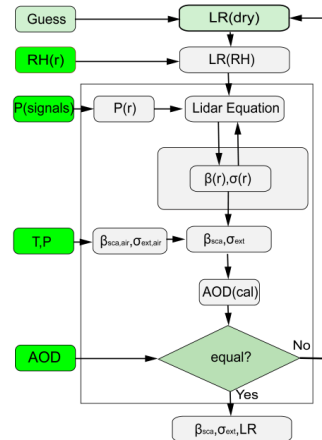
		AOD							
		0.2	0.4	0.6	0.8	1.0	1.2	1.4	1.6
RH profile	P60-70	6	9	11	13	8	8	8	9
	P70-80	7	7	9	12	7	6	7	8
	P80-90	8	5	4	11	6	5	5	6
	P90-95	9	6	6	9	13	7	7	9

498

499



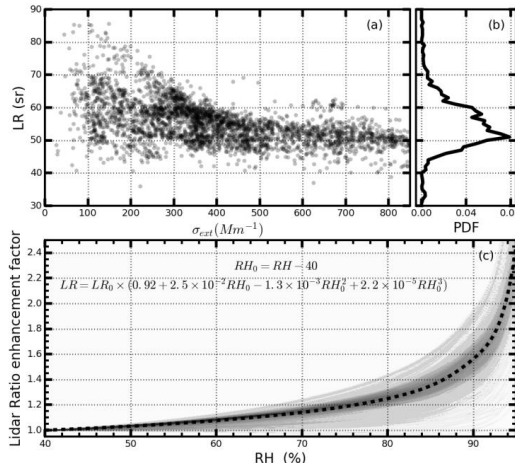
500



501

502 **Figure 1.** Schematic diagram of retrieving the σ_{ext} profile. The input variables are displayed in green background.

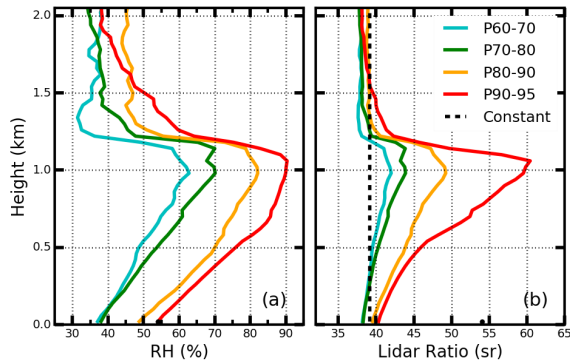
503



504

505 **Figure 2.** LR distribution and LR enhancement factor during Hachi campaign. (a) LR distribution under different
506 polluted conditions. (b) Probability distribution of the LR. (c) Enhancement factor of the LR. Dotted line is the mean
507 fit LR enhancement factor.

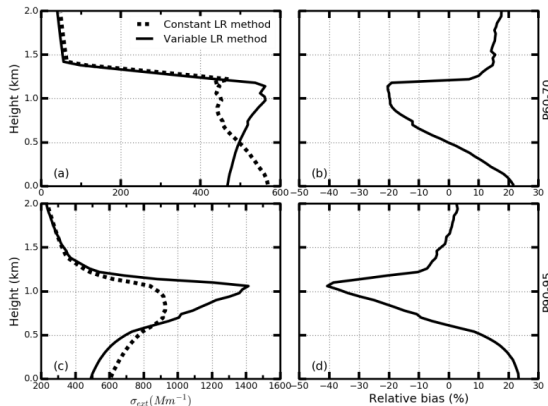
508



509
510 **Figure 3.** (a) Four kinds of RH profiles P60-70, P70-80, P80-90, and P90-95; (b) LR profiles from given RH profiles
511 respectively. Dotted black line is one of the constant LR profile from RH profile of type P70-80 used for retrieving
512 the MPL signals.
513

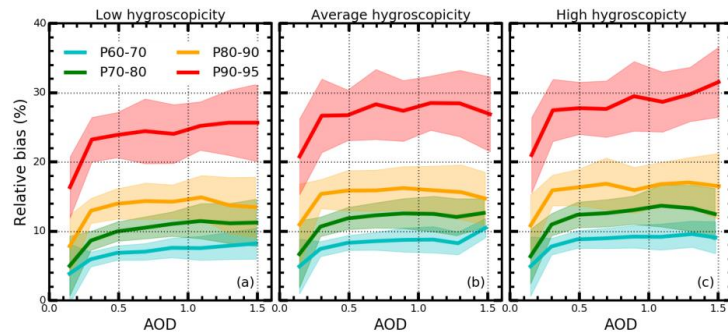


514



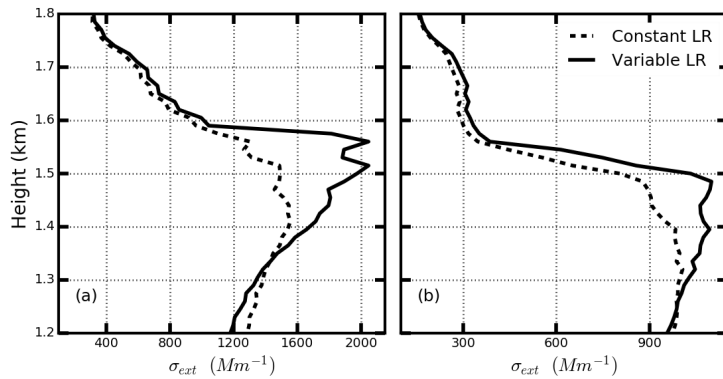
515

516 **Figure 4.** (a) Retrieved σ_{aero} profiles using constant LR profile method (dotted line) and variable LR profile method
517 (solid line). (b) The relative bias of the retrieved σ_{aero} profile using two different methods. (c),(d) are the same as (a),
518 (b) respectively. The LR signals of panel (a) results form P70-80 RH profile, and LR signals of panel (b) results from
519 P90-95 RH profile



520

521 **Figure 5.** Relative bias of the retrieved σ_{ext} under different AOD, PNSD, and hygroscopicity and RH profiles
522 conditions. Different colors represent different RH profile. Panel (a) is derived from the low hygroscopicity. Panel (b)
523 results from the mean hygroscopicity. Panel (c) is for high hygroscopicity.



524

525 **Figure 6.** Retrieved σ_{ext} profiles from field measurement MPL signals at (a) 13:00 and (b) 14:30 on July 5, 2016. Dotted
526 line represents the retrieved σ_{ext} profiles using constant LR profile method. Solid line represents the retrieved σ_{ext} profiles
527 using variable LR profile method.